



Influence of ice crystal shape on retrieval of cirrus optical thickness and effective radius: A case study

H. Eichler,¹ A. Ehrlich,² M. Wendisch,² G. Mioche,³ J.-F. Gayet,³
M. Wirth,⁴ C. Emde,⁴ and A. Minikin⁴

Received 8 April 2009; revised 16 June 2009; accepted 13 July 2009; published 3 October 2009.

[1] Airborne measurements of spectral upwelling radiances (350–2200 nm) reflected by cirrus using the Spectral Modular Airborne Radiation measurement system (SMART)-Albedometer were made over land and water surfaces. Based on these data, cloud optical thickness τ and effective radius R_{eff} of the observed cirrus were retrieved. By using different crystal shape assumptions (hexagonal plates, solid and hollow columns, rough aggregates, planar and spatial rosettes, ice spheres, and a mixture of particle habits) in the retrieval, the influence of crystal shape on the retrieved τ and R_{eff} was evaluated. With relative differences of up to 70%, the influence of particle habit on τ is larger than on R_{eff} (up to 20% differences). Retrieved τ values agreed with values derived from concurrent lidar measurements within the measurement uncertainties.

Citation: Eichler, H., A. Ehrlich, M. Wendisch, G. Mioche, J.-F. Gayet, M. Wirth, C. Emde, and A. Minikin (2009), Influence of ice crystal shape on retrieval of cirrus optical thickness and effective radius: A case study, *J. Geophys. Res.*, 114, D19203, doi:10.1029/2009JD012215.

1. Introduction

[2] Cirrus clouds influence the local and global radiation energy budget by reflecting and absorbing solar radiation as well as by absorbing and emitting thermal infrared radiation [e.g., Liou, 1986; Cess *et al.*, 1993; Chen *et al.*, 2000; Lynch *et al.*, 2002]. The radiative effects of ice clouds on the climate system depend on their optical and microphysical properties [Stephens *et al.*, 1990; Zhang *et al.*, 1999; McFarquhar *et al.*, 2002]. Besides geometric cloud height and thickness, ice water content, and ice crystal size, the ice crystal shape is an important factor influencing the radiative properties of cirrus [e.g., Macke and Francis, 1998; Wyser, 1999; Wendisch *et al.*, 2005]. This owes to the fact that the single-scattering properties of nonspherical ice crystals may differ substantially from those of surface, cross-sectional or volume equivalent spheres [Kinne and Liou, 1989; Takano and Liou, 1989; Macke, 1993]. Contrarily, in global climate models cirrus are mostly represented by a fixed ice particle size and shape [Francis *et al.*, 1998; Garrett *et al.*, 2003]. However, as observed in several field experiments, a variety of ice crystal sizes and shapes exist [Garrett *et al.*, 2003; Lawson *et al.*, 2006; Schmitt and Heymsfield, 2007].

[3] Therefore assumptions on the ice crystal shape are necessary for the retrieval of microphysical properties of cirrus from remote sensing measurements. The retrieved parameters such as cirrus optical thickness τ and cloud effective radius R_{eff} may vary substantially due to the shape assumption [Nasiri *et al.*, 2002]. Especially for optically thin cirrus, for example, Comstock *et al.* [2007] ascertained difficulties in the retrieval of ice crystal shape and size distribution. In addition, the ice crystal surface roughness and inhomogeneities such as inclusions of air bubbles within the ice crystals were found to be of importance in cirrus retrievals [Labonnote *et al.*, 2000; Yang *et al.*, 2008].

[4] The common retrieval technique to derive R_{eff} and τ of water clouds uses measurements of solar radiation reflected by clouds at two wavelengths (bispectral reflectance measurements). It was introduced by Twomey and Seton [1980] and Nakajima and King [1990]. A similar approach using measurements of solar radiation reflected by clouds has been adopted to retrieve cirrus properties [Ou *et al.*, 1993; Rolland *et al.*, 2000; King *et al.*, 2004].

[5] In the works of Francis *et al.* [1998], McFarlane *et al.* [2005], and McFarlane and Marchand [2008], the impact of ice crystal shape on the retrieval of R_{eff} and τ was investigated. Francis *et al.* [1998] applied two near-infrared wavelengths (1.04 μm and 1.55 μm) of a multi-channel radiometer onboard the United Kingdom (UK) Meteorological Office's C-130 aircraft for the retrieval and tested the influence of four crystal habits (ice spheres, hexagonal columns, hexagonal plates, and randomized polycrystals). Retrieval results for five cirrus cases situated over a water surface were compared with in situ measurements. Retrieved R_{eff} and τ depended strongly on assumed particle habit. The assumption of plates and spheres gave highest τ and smallest R_{eff} . Polycrystals were found to

¹Institut für Physik der Atmosphäre, Johannes Gutenberg-Universität Mainz, Mainz, Germany.

²Institut für Meteorologie, Universität Leipzig, Leipzig, Germany.

³Laboratoire de Météorologie Physique, Université Blaise Pascal, Clermont-Ferrand, France.

⁴Institut für Physik der Atmosphäre, Deutsches Zentrum für Luft- und Raumfahrt Oberpfaffenhofen, Wessling, Germany.

Table 1. Overview of Flights Performed During the CIRCLE-2 Field Experiment in May 2007^a

Date	Route	Cloud Type	Aircraft	CloudSat/CALIPSO Interception
13 May	Creil-Creil	Convective clouds	F	Yes
14 May	OP-Leipzig	Broken Ci	G	Yes
14 May	Leipzig-OP	Broken Ci	G	No
16 May	OP-Brest	Frontal Ci	G	No
16 May	Brest-Brest	Frontal Ci	F + G	Yes
16 May	Brest-OP	Frontal Ci	G	No
17 May	OP-OP	Sc	G	No
20 May	Creil-Creil	Broken Ci	F	Yes
20 May	OP-OP	Outflow Ci	G	No
22 May	OP-Esbjerg	Frontal Ci	G	No
22 May	Esbjerg-OP	Frontal Ci	G	No
23 May	OP-Bilbao	Outflow Ci	G	No
23 May	Bilbao-Bilbao	Outflow Ci	G	Yes
23 May	Bilbao-OP	Outflow Ci	G	No
25 May	OP-Brest	Broken Ci	G	No
25 May	Brest-Brest	Ci layer	F + G	Yes
25 May	Brest-OP	Outflow Ci	G	No
26 May	Brest-OP	Outflow Ci	F	No
26 May	OP-OP	Outflow Ci	F + G	Yes
26 May	OP-Brest	Outflow Ci	F	No

^aCloud type Ci and Sc denote cirrus and strato cumulus, respectively. OP is Oberpfaffenhofen, F refers to the French Falcon aircraft, and G to the German Falcon aircraft. Geographical coordinates of the locations are as follows: Bilbao (43.3°N, 2.93°W), Brest (48.45°N, 4.42°W), Creil (49.25°N, 2.5°E), Esbjerg (55.53°N, 8.57°E), Leipzig (51.33°N, 12.38°E), OP (48.08°N, 11.28°E).

give the most consistent agreement with the in situ measurements. The work of *McFarlane et al.* [2005] is based on radiances measured by satellite and focuses on the retrieval of cloud phase and dominant crystal habit. Channel 1 (0.45 μm) of the Multiangle Imaging Spectroradiometer (MISR) onboard the Terra satellite of the Earth Observing System (EOS) as well as channel 7 (2.13 μm) of the Moderate Resolution Imaging Spectroradiometer (MODIS) were used in the retrieval. Seven crystal habits (hexagonal plates, solid and hollow columns, rough and smooth aggregates, spatial and planar rosettes) as well as spherical water droplets were considered. The introduced shape retrieval is based on differences in the phase function of various particle shapes as a function of scattering angle observed under the nine MISR viewing angles. The case studies presented by *McFarlane et al.* [2005] include two cirrus cases observed over land. Depending on the assumed crystal shape, retrieved τ and R_{eff} differed by up to 50% and 30%, respectively. In the work of *McFarlane and Marchand* [2008], statistics of retrieved cloud phase and ice crystal habit based on the algorithm introduced by *McFarlane et al.* [2005] are presented for a data set of five years collected at the Atmospheric Radiation Measurement (ARM) Program's Southern Great Plains (SGP) site. Strongest differences were found between the assumptions of rough aggregates and plates. Statistical analysis showed that 50% of the cirrus were classified as consisting of mostly rough aggregates while the other crystal habits were each dominant in 14–18% of the ice clouds.

[6] In contrast to the publications by *Francis et al.* [1998], *McFarlane et al.* [2005], and *McFarlane and Marchand* [2008], we will not focus on cirrus observed over one specific surface type but instead present cirrus retrieval results over land and open water surfaces. The data are based on

airborne upwelling (cirrus reflected) spectral radiance measurements collected during the CIRrus CLOUD Experiment-2 (CIRCLE-2). The influence of assumed crystal shape on the retrieval of τ and R_{eff} is the central objective of this paper. In addition to seven single particle habit assumptions (hexagonal plates, solid and hollow columns, rough aggregates, spatial and planar rosettes, and ice spheres) a mixture of particle habits as described in the ice cloud parameterization of *Baum et al.* [2005b] is used in our retrieval.

[7] An overview of the field measurements and instrumentation is given in section 2. The cloud retrieval technique applied to derive τ and R_{eff} from a wavelength pair of spectral cloud top reflectances is described in section 3. For two case studies, the retrieval algorithm is applied using different shape assumptions and thus the influence of ice particle habit on the retrieved properties is quantified in section 4. The retrieved τ data are compared to corresponding values of τ from concurrent lidar measurements. In section 5 the conclusions of this paper are given.

2. Experimental

2.1. Overview of the CIRCLE-2 Measurement Campaign

[8] Data presented here were obtained during the CIRCLE-2 field campaign in May 2007. This experiment focused on the airborne measurement of radiative and microphysical properties of cirrus to validate retrieval algorithms based on satellite measurements, in particular of Meteosat Second Generation (MSG) and CALIPSO/CloudSat of the A-Train [*Stephens et al.*, 2002]. Airborne measurements were conducted with two research aircraft: a German Falcon 20 operated by Deutsches Zentrum für Luft- und Raumfahrt (DLR) and a French Falcon 20 operated by SAFIRE (Service des Avions Français Instrumentés pour la Recherche en Environnement). Both aircraft were equipped with lidars (light detection and ranging) in nadir looking configuration. In addition, in situ measurements of cloud and aerosol properties as well as upwelling spectral radiances were made onboard the German Falcon while the French Falcon also carried a radar system.

[9] In total, 20 flights were performed over continental Europe, the North Sea, and the Atlantic Ocean as summarized in Table 1. The time period of the aircraft operation was limited to about two weeks. Therefore a rather large operational area was required in order to meet the best possible meteorological situations for cirrus observations, combined with the location of the daytime CALIPSO/CloudSat overpass tracks and restrictions imposed by air traffic control (ATC) in different European countries. The preferred meteorological conditions were single-layer cirrus clouds over water surfaces. At the same time, the cirrus cloud altitudes were required to be low enough for the aircraft to fly above the cirrus for the lidar and reflectance measurements. For flight planning customized products of ECMWF (European Centre for Medium-Range Weather Forecasts) forecast data as well as MSG images were used.

[10] During three missions (see Table 1) both Falcon aircraft were flying in close coordination. The French Falcon was flying above clouds for lidar and radar observations while the German Falcon was positioned below the French Falcon for in situ measurements inside the cirrus

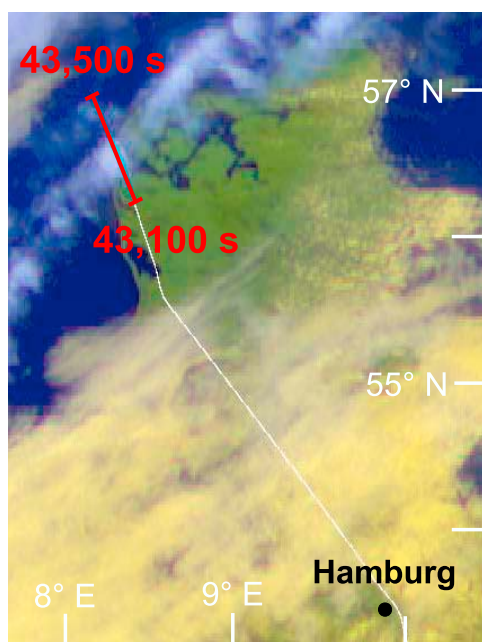


Figure 1. False color composite using MSG-SEVIRI channels 1, 2, 9, and 12 of the west coast of Denmark at 12 UTC on 22 May 2007 with superimposed flight track over probed cirrus.

clouds. However, in the two specific cases investigated in this study, the German Falcon was operating alone. The flight strategy in this case was to first fly above the cirrus for the remote sensing measurements, then turn around and fly several legs at different altitudes inside the cloud. This procedure typically caused a time delay between roughly collocated remote sensing and in situ measurements in the range of 5–20 min. As illustrated in Table 1, the aircraft cirrus measurements were closely collocated with observations of CALIPSO/CloudSat during several missions. Results of these cases are described by G. Mioche et al. (Validation of the CALIPSO/CALIOP extinction coefficients from in situ observations in midlatitude cirrus clouds during CIRCLE-2 experiment, submitted to *Journal of Geophysical Research*, 2009).

2.2. Instrumental

[11] Spectral upwelling radiances I_{λ}^{\uparrow} were measured with the Spectral Modular Airborne Radiation measurement system (SMART)-Albedometer [Wendisch et al., 2001], developed at the Leibniz Institute for Tropospheric Research (IfT), Leipzig, Germany. By connecting specific optical inlets to a set of up to six grating spectrometers, this instrument allows the measurement of different radiometric quantities (irradiance, radiance, actinic radiation) on airborne platforms [Bierwirth et al., 2009]. However, due to operational constraints of the aircraft, only one optical inlet was installed during the CIRCLE-2 experiment. With an opening angle of 2.1° it was designed to measure radiances [Ehrlich et al., 2008] and was connected to two plane grating spectrometers operating in the wavelength ranges 350–1050 nm and 900–2200 nm with spectral resolutions

(Full Width at Half Maximum, FWHM) of 2–3 nm and 9–16 nm, respectively. The radiance inlet was installed on the fuselage of the aircraft in approximately nadir looking configuration (deviation from nadir $4\text{--}5^{\circ}$). The temporal resolution of the radiance measurement is about 0.5 s leading to an averaging of 100 m at an aircraft velocity of 200 m s^{-1} . Error estimations for (I_{λ}^{\uparrow}) include calibration lamp and transfer calibration uncertainties (between laboratory and field) as well as the wavelength accuracy of the spectrometers. Resulting total relative errors are wavelength dependent and are in the range of 6% for 635 nm and 9% for 810 nm and 1640 nm, respectively.

[12] With WALES (Water vapor Lidar Experiment in Space), the multi-wavelength water vapor differential absorption lidar operated by DLR onboard the German Falcon, lidar signal backscatter ratios at 1064 nm wavelength were measured [Wirth et al., 2009]. An extinction correction of the data was applied assuming a backscatter-to-extinction ratio of 20 sr which is a typical value for cirrus in the northern hemisphere at this wavelength. The Klett inversion method [Klett, 1981] was used to determine τ from the lidar data. Due to the exponential increase of the error for cirrus with increasing τ , lidar-derived τ were reliable for optically thin clouds only. For optically thin cirrus with $\tau < 2$, uncertainties in derived τ are estimated as 20–30%.

[13] Onboard the DLR Falcon aircraft, microphysical in situ measurements such as ice particle number size distributions and ice particle concentrations were obtained by a Forward Scattering Spectrometer Probe (FSSP-300, size range 3–20 μm [Baumgardner et al., 1992]) operated by DLR and a Cloud Particle Imager (CPI, size range 20–2300 μm [Lawson et al., 2001]) operated by the Laboratoire de Météorologie Physique, Université Blaise Pascal (LaMP), Clermont Ferrand, France. Ice crystal shapes were determined in postprocessing of the CPI images. However, due to the unknown magnitude of measuring artifacts caused by particle shattering on microphysical probes, R_{eff} were not determined from these in situ measurements.

2.3. Case Study of 22 May 2007

[14] We present results from two case studies based on the first flight performed on 22 May 2007. This day was chosen for detailed analysis because single-layer cirrus was observed. Frontal cirrus associated with a low pressure system centered over Iceland was advected to Denmark from westerly directions. Only one aircraft (the German Falcon) was operated that day. The flight track led along the West Coast of Jutland, Denmark, where an inhomogeneous, thin and narrow cirrus band was present in 7–10.4 km altitude around 12 UTC (43,200 s). The cirrus is shown in the MSG image (Figure 1) and in the time series of attenuated backscatter ratio at 1064 nm wavelength in Figure 2. The flight leg above the cirrus at an altitude of 10.7 km and Northwestern direction was followed by an in-cloud flight leg for microphysical measurements at different altitudes (shown here: uppermost leg at 9.78 km) during which the Falcon was flying in a Southeastern direction. The retrieval of τ and R_{eff} was realized for parts of the cirrus over land during which the geometrical thickness of the cirrus was nearly constant (43,146–43,220 s) referred to as period P1 as well as for the cirrus over water denoted as

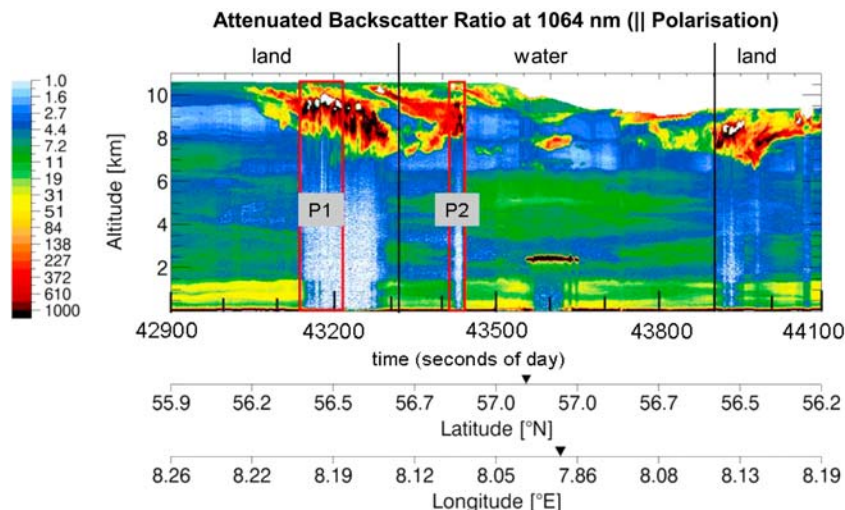


Figure 2. Attenuated backscatter ratio at a wavelength of 1064 nm from the DLR-lidar of flight 22 May 2007 (42,900–44,100 s). The area between the black vertical lines indicate the flight leg over the North Sea, the red boxes show the time spans for which cloud retrievals were made (P1 = 43,146–43,220 s, P2 = 43,419–43,435 s). Latitude and longitude of the flight track are included below the graph, turns are indicated by black triangles.

period P2 (43,419–43,435 s). Both periods are highlighted in Figure 2 with red boxes. In addition, the flight leg over water is indicated by the area between the black vertical lines. Apart from the encounter with the water cloud in about 2 km height at 43,580–43,650 s which did not overlap with the chosen time periods for the cirrus retrieval no clouds at lower level were present.

[15] Time series of upwelling radiances measured at three wavelengths (635 nm, 810 nm and 1640 nm) during 43,000–43,500 s (11:56–12:05 UTC) corresponding to the flight leg in nearly 11 km height (above cloud) are presented in Figure 3 in which P1 and P2 are indicated as well. The wavelengths 635 nm, and 1640 nm were chosen because they are used for the cirrus retrieval while at 810 nm the influence of surface albedo is illustrated.

[16] In Figure 3, the cirrus can be identified by the high values of I_{λ}^{\uparrow} at around 43,120–43,300 s (including P1). This cirrus was situated over land. As obvious in the variations of I_{λ}^{\uparrow} during the cloud-free time before 43,120 s as well as in photographs taken during the flight, the surface albedo varied considerably because land use over this part of the Danish West Coast is quite diverse. Over vegetated areas, the surface albedo increases sharply at about 700–800 nm wavelength leading to increased I_{λ}^{\uparrow} for cloud-free times (43,000–43,120 s) at 810 nm. Following the flight leg over land, the aircraft track led over open water, where the surface albedo is low. Thus I_{λ}^{\uparrow} over an optically very thin cirrus (43,300–43,400 s) is small and does not exceed $0.02 \text{ W m}^{-2} \text{ nm}^{-1} \text{ sr}^{-1}$ at 635 nm wavelength. For a short period over open water (P2) a thicker patch of cirrus was encountered resulting in a sharp peak in I_{λ}^{\uparrow} .

3. Methodology

3.1. Retrieval of Microphysical and Optical Cirrus Properties

[17] The cirrus retrieval described subsequently follows the common bispectral reflectance technique introduced by

Nakajima and King [1990]. The spectral cloud top reflectance is determined by

$$R(\lambda) = \pi \cdot I_{\lambda}^{\uparrow} / F_{\lambda}^{\downarrow}. \quad (1)$$

[18] Time series of cirrus spectral cloud top reflectances $R_{\text{meas}}(\lambda)$ were derived from SMART-Albedometer measurements. Therefore measured I_{λ}^{\uparrow} were complemented by calculated downwelling spectral irradiances F_{λ}^{\downarrow} at flight level. F_{λ}^{\downarrow} were determined by one-dimensional radiative transfer simulations with libRadtran (the library of Radiative transfer [Mayer and Kylling, 2005]).

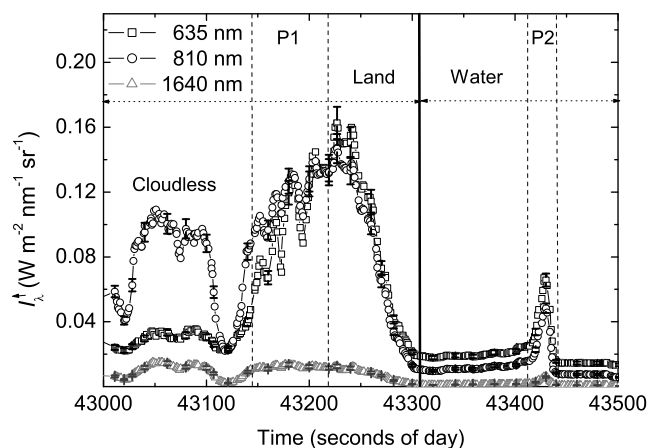


Figure 3. Time series of upwelling radiances I_{λ}^{\uparrow} measured with the SMART-Albedometer at different wavelengths for the radiation leg of flight 22 May 2007 (43,000–43,500 s) over Jutland and the North Sea. Error bars representing measurement and calibration uncertainties are included. Dashed vertical lines indicate cloud retrieval periods P1 and P2, to the right of the solid black line the aircraft was over the North Sea.

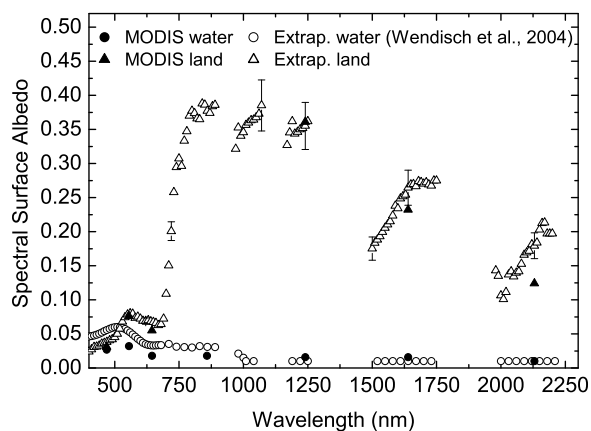


Figure 4. Spectral surface albedos of land and water as used in the cloud retrieval for P1 and P2, respectively. Surface albedos obtained from MODIS are also presented.

[19] Pseudospectral calculations were made using the so-called correlated- k approximation in which the gas absorption parameterization SBDART [Ricchiuzzi *et al.* [1998]] is adopted. As radiative transfer equation solver the plane-parallel discrete ordinate DISORT2 algorithm by Stamnes *et al.* [1988] was employed in which 16 streams were used for the calculations.

[20] Using the ice cloud parameterization by Key *et al.* [2002] as input to the radiative transfer model, lookup tables of modeled spectral cloud top reflectances $R_{\text{mod}}(\lambda)$ were generated for sets of cirrus optical thickness and effective radius (for P1 $\tau = 0.1\text{--}8.1$, $\Delta\tau = 0.5$, $R_{\text{eff}} = 5\text{--}35\ \mu\text{m}$, $\Delta R_{\text{eff}} = 5\ \mu\text{m}$, see Figure 5; for P2 $\tau = 0.1\text{--}3.6$, $\Delta\tau = 0.5$, $R_{\text{eff}} = 5\text{--}35\ \mu\text{m}$, $\Delta R_{\text{eff}} = 5\ \mu\text{m}$, see Figure 6). In the Key parameterization optical properties (ice crystal volume extinction coefficient, asymmetry parameter, and single-scattering albedo) for different particle habits (hexagonal plates, rough aggregates, solid and hollow columns, planar and spatial rosettes) are parameterized as function of ice water content (IWC) and R_{eff} . In the Key parameterization the effective radius is defined as

$$R_{\text{eff}} = \frac{3}{4} \frac{\int_{L_{\text{min}}}^{L_{\text{max}}} V(L) \cdot n(L) dL}{\int_{L_{\text{min}}}^{L_{\text{max}}} A(L) \cdot n(L) dL} \quad (2)$$

where L is the maximum dimension of an ice crystal, $n(L)$ is the number concentration of particles with maximum dimension L in the size distribution, V and A are the volume and mean projected area of the particles, respectively. The volume and area are based on the spherical diameter with equivalent volume and the spherical diameter with equivalent projected area as defined by Yang *et al.* [2000].

[21] In the Key parameterization optical properties are integrated over 56 spectral bands ranging from 0.2 to 5.0 μm , the wavelength bands used for the cloud retrieval are 0.6–0.7 μm and 1.5–1.65 μm . In the first band, ice is almost nonabsorbing and the reflectance largely depends on cirrus τ . In the second band ice crystals strongly absorb solar

radiation as function of R_{eff} ; it thus provides information on particle size. In order to compare $R_{\text{mod}}(\lambda)$ and $R_{\text{meas}}(\lambda)$, measured values were also averaged over the two spectral bands.

[22] Furthermore, lookup tables were calculated using the ice crystal parameterization of Baum *et al.* [2005a, 2005b] which is also used in the MODIS retrievals of τ and R_{eff} . This parameterization is a library of optical properties based on 1117 particle number size distributions obtained from aircraft in situ measurements in midlatitude and tropical cirrus during various field experiments. Instead of dealing with single particle habits, the optical properties in this parameterization are described for particle-size-dependent habit mixtures consisting of droxtals, hexagonal plates, solid columns, hollow columns, aggregates, and spatial bullet rosettes. The library of scattering properties covers 234 discrete wavelengths between 0.4 and 13 μm in increments of 0.01 μm /0.05 μm for wavelengths smaller/larger than 2.2 μm . Among others, optical properties of the ice crystals such as asymmetry parameter, extinction cross section and single-scattering albedo over a broad range of particle sizes (2–9500 μm) are included in the database.

[23] Finally, for reasons of comparison, also spherical ice particles were used to calculate lookup tables of $R_{\text{mod}}(\lambda)$. The single scattering properties of ice spheres were taken from precalculated tables of optical properties based on Mie theory which are part of the libRadtran software package.

3.2. Spectral Surface Albedo

[24] The spectral surface albedo is a crucial input to cloud retrieval algorithms which are based on cloud-reflected solar radiation [Rolland *et al.*, 2000], especially for optically thin cirrus above strongly reflecting surfaces. Therefore we used surface albedo spectra derived from clear sky SMART-Albedometer measurements made in the vicinity of the cirrus in the simulations when possible. As obvious in Figure 2, P1 was preceded by a cloudless part (42,900–43,120 s) for which the mean spectral surface albedo was derived as follows: The algorithm for nonlinear extrapolation of the surface albedo from clear sky airborne spectral radiation measurements at a certain flight altitude adapted from the work of Wendisch *et al.* [2004] was applied. While irradiances were used in the work of Wendisch *et al.* [2004], we adjusted the algorithm to spectral radiances I_{λ} . Describing the adaptation of the algorithm in detail is beyond the scope of this work. As explained by Bierwirth *et al.* [2009], gas absorption bands in which the measurement signal is strongly attenuated are critical for the extrapolation. For that reason, the following bands corresponding to oxygen and water vapor absorption bands were excluded from the surface albedo extrapolation results: 750–775 nm, 890–970 nm, 1080–1170 nm, 1260–1500 nm, 1750–1975 nm. The resulting spectral surface albedo used for the cirrus retrieval simulations of P1 is shown in Figure 4. Since no clear sky period was encountered over water (see Figure 2), the water albedo for shallow coastal waters with high spectral resolution as determined by Wendisch *et al.* [2004] was employed in the cirrus retrieval simulations for P2 (see Figure 4).

[25] In Figure 4 the surface albedos derived from seven MODIS bands [Schaaf *et al.*, 2002] at the corresponding locations are also presented. While extrapolated surface

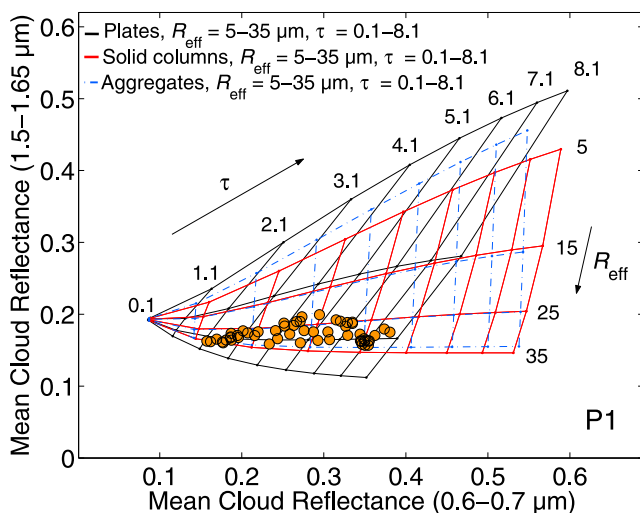


Figure 5. Cloud retrieval solution space for three particle habits showing isolines of constant τ and R_{eff} (in μm). Observed cloud top reflectances of the first flight on 22 May 2007 (period 1 (P1), 43,146–43,220 s) over land are represented by dots.

albedos are based on short time periods of clear sky measurements of I_{λ}^{\uparrow} , MODIS surface albedo products comprise averages of a 16-day measurement period. Despite this difference, the instantaneous extrapolated spectral surface albedo over land and the MODIS-derived values mostly agree within the error bars of the surface albedo extrapolation. Above open water the MODIS albedo at wavelengths below 1000 nm is smaller than the one with high-spectral resolution. This can partly be explained by wind-speed-dependent wave action influencing the surface albedo and by the fact that the albedo measurement of *Wendisch et al.* [2004] was made over the coastal waters of Florida while here the flight track led over the coastal waters of the North Sea. Still, when comparing measured and modeled I_{λ}^{\uparrow} assuming the extrapolated water albedo from the work of *Wendisch et al.* [2004] values were found to agree within the measurement uncertainty of I_{λ}^{\uparrow} and can thereby be used in the cirrus retrieval simulations of P2. In that context, it should be noted that for the wavelength range 600–1650 nm, which is of importance for the cirrus retrieval, the albedo of water is much lower than that of vegetated land surfaces and for that reason less crucial because it contributes much less to I_{λ}^{\uparrow} above the cirrus.

4. Cloud Retrieval Results and Discussion

4.1. Lookup Tables

[26] In the following, results of the cloud retrieval are presented. Radiative transfer calculations for the respective solar zenith angle of 37° were performed for six different ice crystal habits available for the *Key* ice cloud parameterization, the mixture of ice crystal habits of the parameterization by *Baum et al.* [2005b], and for ice spheres. When varying the ice crystal shape while keeping τ and R_{eff} constant, differences of $R_{\text{mod}}(\lambda)$ will result only from differences in the scattering phase function of the different crystal habits. Separate lookup tables were calculated for both the land and water surface albedo for each of the assumed crystal shapes.

They are illustrated in Figures 5 and 6 along with $R_{\text{meas}}(\lambda)$. The data of the lookup tables (pairs of $R_{\text{mod}}(\lambda)$ which are averaged over the wavelength bands 0.6–0.7 μm and 1.5–1.65 μm) generate a two-dimensional solution space which is characterized by isolines of τ (rather horizontal lines) and R_{eff} (almost vertical lines). Each pair of $R_{\text{meas}}(\lambda)$ corresponds to a pair of τ and R_{eff} .

[27] Increasing τ (e.g., 0.1–8.1 in Figure 5 and 0.1–3.6 in Figure 6) results in increasing $R(\lambda)$ in the nonabsorbing wavelength range 0.6–0.7 μm , while increasing R_{eff} (e.g., 5–35 μm in Figures 5 and 6) leads to decreasing $R(\lambda)$ at the absorbing wavelength range 1.5–1.65 μm . Via interpolation of modeled cloud top reflectances to the observed cloud top reflectance values, time series of τ and R_{eff} for the presented cirrus were derived. Statistics and time series of the retrieved values are shown in Table 2, Table 3, and Figure 7, respectively. There, the results are compared to independent estimates of τ and R_{eff} derived from lidar and microphysical in situ measurements.

[28] The uncertainties of I_{λ}^{\uparrow} are considered in the interpretation of the cloud retrieval results. To estimate the uncertainty of the retrieved values, τ and R_{eff} were retrieved for the I_{λ}^{\uparrow} which was varied in positive and negative direction according to the calibration uncertainty of the I_{λ}^{\uparrow} measurement (6% and 9% at 0.6–0.7 μm and 1.5–1.65 μm , respectively). As an average over all habits, an error of 8% and 9% in τ and R_{eff} , respectively was estimated (see Table 4).

4.2. Shape Effects on Retrieved τ

[29] Mean retrieved τ of P1, denoting the part of the cirrus above Jutland, range from 3.0 for solid columns and rough aggregates to 4.9 for hexagonal plates (see Table 2). Only spheres yield even larger τ averaging at 5.5. Results assuming spherical ice crystals are less realistic and only shown here for comparison. Retrieved τ of all other habits range between the mentioned extreme values. Assuming a

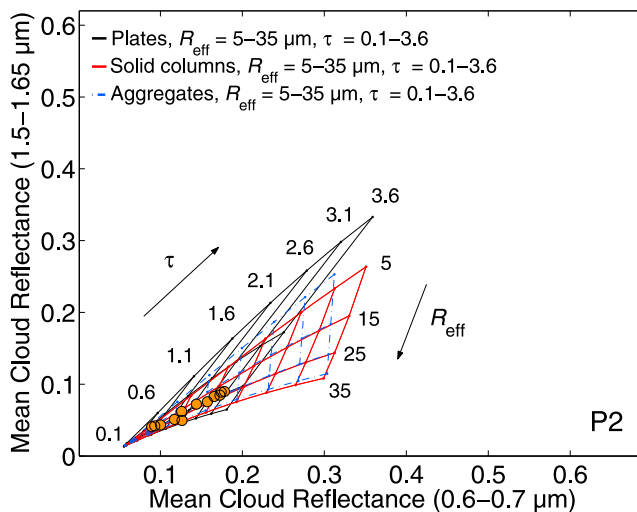


Figure 6. Cloud retrieval solution space for three particle habits showing isolines of constant τ and R_{eff} (in μm). Observed cloud top reflectances of the first flight on 22 May 2007 (period 2 (P2), 43,419–43,435 s) above the North Sea are represented by dots.

Table 2. Retrieved τ and R_{eff} for Flight 22 May 2007 (P1, 43146–43220 s) Over Land and τ Values Derived From Lidar Measurements (SD, standard deviation)

	τ		$R_{\text{eff}} (\mu\text{m})$	
	Mean	SD	Mean	SD
Hexagonal plates	4.9	1.7	24.5	1.8
Solid columns	3.0	1.0	29.2	3.4
Rough aggregates	3.0	1.0	29.7	4.0
Hollow columns	3.7	1.2	23.2	2.4
Planar rosettes	3.7	1.2	24.0	2.5
Spatial rosettes	3.5	1.2	23.6	2.4
Mix	3.4	1.2	29.7	3.5
Ice spheres	5.5	1.9	26.2	3.1
Lidar	(1.9)	(0.4)	–	–

mixture of crystal shapes, $R_{\text{meas}}(\lambda)$ fit best with $R_{\text{mod}}(\lambda)$ assuming cirrus with τ of 3.4 on average. For cirrus with $\tau > 2$ no reliable τ values can be derived from lidar measurements due to its limited dynamical range. For that reason, the lidar-derived values are not comparable for P1 where τ derived from $R(\lambda)$ are higher than 2.

[30] Comparing retrieved τ under different crystal shape assumptions for P2 when the cloud was optically thinner leads to similar results as during P1. As presented in Table 3, largest values of τ are derived assuming spheres (mean = 2.3), followed by hexagonal plates (mean = 2.1) while the lower end of the scale is established assuming solid columns (mean = 1.2), rough aggregates, and a mixture of habits (both with means of 1.3). Lidar-derived τ of 1.7 ± 0.6 agree well with the values derived from reflectance measurements. As a result of the spatial inhomogeneity of the cirrus, the retrieved τ of one particle habit vary by a factor of about 3–4 during P1 and P2 (see Figure 7a and 7c). With the help of the lidar a crystal shape retrieval might be possible (see Figure 7c): During the first half of the short cirrus encounter lidar-derived τ agree with results for solid columns and a mixture of particle habits. During the second half of the time series, τ values from lidar measurements are more similar to the assumption of hexagonal plates. Crystal shapes determined from remote sensing methods are only representative for the uppermost cirrus layer where single scattering dominates. As discussed by *Chepfer et al.* [2002] and *Wendisch et al.* [2005] the differences of scattering phase functions of varying crystal habits diminish due to multiple scattering for $\tau > 2$. For that reason, only comparisons with in situ measurements in the upper parts of the cirrus were made. CPI images show that at the uppermost in-cloud flight leg at 9.78 km a mixture of different ice particle habits was observed: plates, columns, and rosettes are the main distinguishable shapes. However, the contribution of irregularly shaped particles is dominant. This probably results from the fact that the shape of particles smaller than $50 \mu\text{m}$ cannot be confidently determined from the analysis of CPI images [*Korolev et al.*, 1999] and are therefore frequently classified as irregulars. Even though CPI images mostly correctly discriminate large crystals ($R_{\text{eff}} > 50 \mu\text{m}$), it is reasonable to assume that also small crystals of the identified shapes exist. Therefore it is stated that these microphysical measurements of crystal shapes support the findings of the combined retrieval of τ from lidar and radiance measurements. However, the authors want to emphasize that due to the combined uncertainties of lidar

and radiance measurements reliable retrievals of dominant ice crystal shape are not possible.

4.3. Shape Effects on Retrieved R_{eff}

[31] Retrieval results of R_{eff} for P1 (see Table 2) show smallest values assuming hollow columns, rosettes, and plates with mean values of 23–24.5 μm . They are about 15–20% smaller than the values assuming solid columns, rough aggregates, or a mixture of habits for which highest R_{eff} (means around 29–30 μm) were retrieved. The assumption of spherical ice particles leads to mean R_{eff} of about 26 μm . As shown in Figure 7b, spatial variations of R_{eff} (about 40%) during P1 are smaller than variations of τ .

[32] Similar to P1, the results for P2 in Table 3 show that smallest R_{eff} were derived assuming hollow columns or rosettes. For these habits, $R_{\text{meas}}(\lambda)$ fit best with $R_{\text{mod}}(\lambda)$ assuming cirrus with R_{eff} of 18–19 μm on average. In contrast to P1, retrieved R_{eff} assuming hexagonal plates with a mean of nearly 25 μm are about 20% larger than the values retrieved for solid columns (mean = 20.6 μm). Again, mean R_{eff} values for aggregates and a mixture of particle habits are very similar (means of roughly 23 μm) but slightly higher than the ones of solid columns. Under the rather unrealistic assumption of spherical particles, mean retrieved R_{eff} amount to 28.7 μm . During the 3 km flight leg of P2 R_{eff} values vary by a factor of three due to spatial cirrus inhomogeneities (see Figure 7d).

4.4. Influence of Surface Albedo Type and Position of $R_{\text{mod}}(\lambda)$ in the Lookup Tables

[33] As illustrated in Figures 5 and 6, the shape of the cloud retrieval solution grid strongly depends on surface albedo. For that reason the influence of a surface albedo variation by 10% was tested. As an average over all crystal habits and both periods, the surface albedo variation was found to lead to uncertainties of about 3% and 6% in τ and R_{eff} , respectively as presented in Table 4.

[34] The assumption of solid columns and hexagonal plates lead to minimum and maximum retrieved values of τ and considerably differences in retrieved R_{eff} (see Tables 2 and 3). As explained by *Francis et al.* [1998], the differences are largely due to the much higher degree of forward scattering of hexagonal plates compared to columns. Also, it should be noted that the location of the data points in the cloud retrieval space, or to be more exact, the mesh density

Table 3. Retrieved τ and R_{eff} for Flight 22 May 2007 (P2, 43419–43435 s) Above the North Sea and τ Values Derived From Lidar Measurements (SD, standard deviation)

	τ		$R_{\text{eff}} (\mu\text{m})$	
	Mean	SD	Mean	SD
Hexagonal plates	2.1	0.8	24.6	3.2
Solid columns	1.2	0.4	20.6	6.1
Rough aggregates	1.3	0.4	22.6	5.7
Hollow columns	1.6	0.6	18.4	4.7
Planar rosettes	1.5	0.5	18.7	4.8
Spatial rosettes	1.5	0.5	18.4	4.7
Mix	1.3	0.5	23.2	4.3
Ice spheres	2.3	0.9	28.7	3.8
Lidar	1.7	0.6	–	–

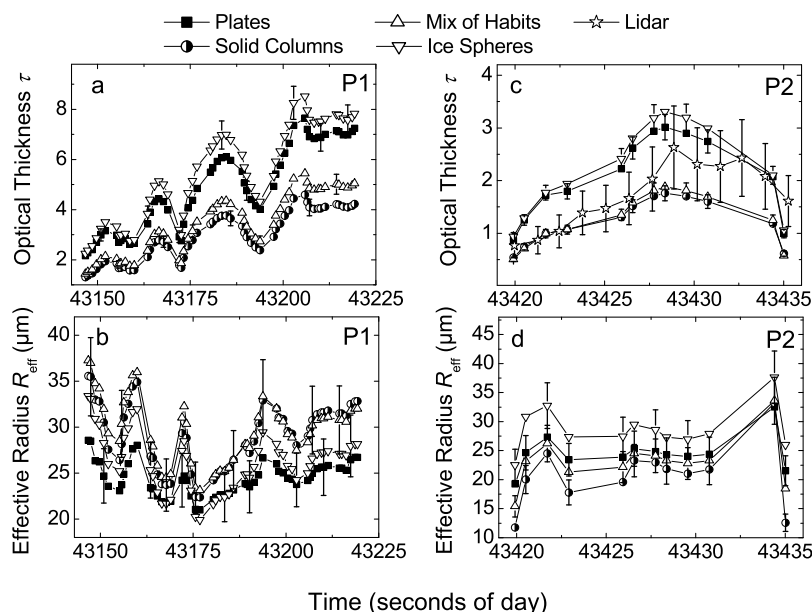


Figure 7. Time series of retrieved optical thickness τ and effective radius R_{eff} for different ice crystal shape assumptions for flight 22 May 2007 (period 1 (P1), 43,146–43,220 s) and (period 2 (P2), 43,419–43,435 s). Lidar-derived τ are also shown (for P2). Error bars based on measurement uncertainties are included. Please note that different y scales are used.

has an influence on the retrieved values. While data points in P1 (see Figure 5) have relatively big reflectances and are thereby situated in the well-spread part of the τ - R_{eff} solution space, the observed reflectances in P2 (see Figure 6) are small and close to the origin of the solution space where constant lines of τ and R_{eff} are very close to each other. This fact in combination with the differing surface albedo in P1 and P2 leading to different shapes of the cloud retrieval solution grid also explains why R_{eff} for hexagonal plates were about 15% smaller in P1 and 20% larger in P2. In addition, as stated by *Knap et al.* [1999], for optically thick clouds retrieved crystal sizes are less uncertain than for optically thin clouds because for increasing values of τ lines of constant τ and R_{eff} are becoming nearly orthogonal.

4.5. Influence of Wavelengths Used in the Retrieval

[35] Finally, the question of which wavelengths can be used in the cirrus retrieval is addressed. As described by *Platnick et al.* [2003], MODIS cirrus retrievals are made at different wavelength combinations. The nonabsorbing band is chosen to minimize the impact of the underlying surface. For land and ocean surfaces the bands at 0.65 μm and 0.86 μm are selected. Moreover, three different bands (1.6 μm , 2.1 μm , and 3.7 μm) sensitive to ice absorption are used. MODIS products based on three retrievals (of the chosen nonabsorbing band in combination with each of the absorbing bands) are available. Since the 3.7 μm band is not covered by our I_{λ}^{\uparrow} measurements, we tested the influence of applying a cirrus retrieval at 0.6–0.7 μm in combination with the 2.1–2.2 μm range. As previously mentioned, optical properties of the Key ice cloud parameterization are integrated over spectral bands; for that reason mean $R(\lambda)$ of the given wavelength ranges are used. For P1 it was found that employing the wavelength range 2.1–2.2 μm

resulted in slightly smaller retrieved τ in comparison to using the 1.5–1.65 μm range. As an average over all crystal habits this difference was 5%. This deviation results from the uncertainties in I_{λ}^{\uparrow} measurements which propagate in the retrieval. Due to the nonperpendicular shape of the reflectance grid uncertainties of I_{λ}^{\uparrow} at ice-absorbing wavelengths cause not only a deviation in the retrieved R_{eff} but also a deviation in τ . The uncertainties of $I_{1.6 \mu\text{m}}^{\uparrow}$ and $I_{2.1 \mu\text{m}}^{\uparrow}$ differ with 9.2% and 10.1%, respectively, causing differences of the retrieval results.

[36] R_{eff} values retrieved by reflectance-based methods correspond to the upper cloud layers [*Platnick*, 2000]. On average, retrieved R_{eff} based on $R(\lambda)$ at 2.1–2.2 μm are 30% smaller than the ones using $R(\lambda)$ at 1.5–1.65 μm . This can be explained by the fact that due to varying strengths of ice crystal absorption at these different spectral bands, the retrieved R_{eff} are representative for different heights within the cloud. Ice absorption at 2.1–2.2 μm is stronger than at 1.5–1.65 μm hence the 2.1–2.2 μm result corresponds to the very top layer while radiation at 1.5–1.65 μm can penetrate somewhat deeper within the cloud.

[37] Several studies on the vertical profile of ice crystal size distributions [e.g., *Francis et al.*, 1998; *Garrett et al.*, 2003; *Gayet et al.*, 2004] found increasing R_{eff} with decreasing height. It is argued that a temperature increase toward lower altitudes causes enhanced water vapor growth and thereby larger crystals. However, as emphasized by

Table 4. Uncertainties of Retrieved τ and R_{eff} Due to I_{λ}^{\uparrow} Measurement Uncertainty and Surface Albedo Variation of 10%

Induced Error in % due to	τ	R_{eff}
I_{λ}^{\uparrow} uncertainty	8	9
Surface albedo variation	3	6

Chang and Li [2003], it is difficult to assign the reflectance-based retrieval results from different wavelengths to any particular cloud level near cloud top. In addition, Platnick [2000] investigated the influence of solar zenith angle on the height within the cloud at which a retrieved R_{eff} is valid. He found that the lower the sun, the shallower the layer into which photons can penetrate thus retrieved R_{eff} at high solar zenith angles correspond to ice particles at higher layers in the cloud than the once retrieved for lower solar zenith angles.

[38] For P2, the retrieval at 0.6–0.7 μm and 2.1–2.2 μm was not made. Instead, the cirrus retrieval was repeated for the nonabsorbing wavelength preferred for clouds over water surfaces (0.86 μm [Knap et al., 1999; Platnick et al., 2003; King et al., 2004]). Using $R(\lambda)$ at 0.8–0.9 μm in combination with the 1.5–1.65 μm band resulted in retrieved τ differing up to 7% from the ones based on $R(\lambda)$ at 0.6–0.7 μm . This is still within the τ uncertainty range induced by I_{λ}^{\uparrow} measurement uncertainties (see Table 4) and thereby justifies that we use 0.6–0.7 μm instead as non-absorbing band to retrieve τ .

5. Summary and Conclusions

[39] Cirrus retrievals of optical thickness τ and particle effective radius R_{eff} on the basis of airborne measurements of upwelling spectral radiances were presented. Data was obtained with the SMART-Albedometer during the CIRCLE-2 aircraft field experiment in May 2007. Spectral cloud top reflectances in a wavelength range for which ice is mostly scattering solar radiation (largely dependent on τ) as well as a spectral band in which ice is absorbing solar radiation (controlled by R_{eff}) were calculated by one-dimensional radiative transfer simulations. By using the ice-cloud parameterizations of Key et al. [2002] and Baum et al. [2005b] as well as optical properties for spherical particles based on Mie theory as input to the model, lookup tables of cloud top reflectances were generated for a range of τ and R_{eff} under the assumption of different ice crystal habits. Retrievals were made for two different surface albedos (land (P1) and water (P2)). Retrieved τ values were compared with lidar-derived τ and found to agree reasonably. Special attention was paid to the influence of assumed crystal shape on the retrieved τ and R_{eff} . The analysis showed that the influence of crystal habit on τ is larger than on R_{eff} . Shape-induced percent differences between retrieved τ may amount up to 70% which is in agreement with McFarlane et al. [2005] and Key et al. [2002] stating differences of up to 50% and 60%, respectively. With maximum differences in retrieved R_{eff} of about 20% our results are of the same magnitude as the ones reported by Knap et al. [1999] (11%) and McFarlane et al. [2005] (30%). These findings highlight the need for using reasonable crystal habit assumptions in remote sensing retrievals of τ and R_{eff} .

[40] Formenti and Wendisch [2008] emphasize that aircraft measurements and satellite observations are synergistic tools both having their own strengths and weaknesses. Presented airborne spectral radiance measurements above cirrus with concurrent lidar and microphysical measurements provide a good tool to verify satellite cirrus retrieval algorithms of τ and R_{eff} . Comparisons of our retrieval

results with optical and microphysical properties derived from MSG and CALIPSO are planned.

[41] **Acknowledgments.** This work was conducted within the scope of the Collaborative Research Center 641: TROPICE “The Tropospheric Ice Phase”. We thank Ulrich Hamann, Luca Bugliaro, and Bernhard Mayer of DLR for providing surface albedo data from MODIS, the MSG image, and support with libRadtran, respectively. The work of the DLR flight operations team and the Falcon pilots is also acknowledged. Jost Heintzenberg is thanked for supporting the developed of the SMART-Albedometer at the Leibniz Institute for Tropospheric Research (IfT), Leipzig, Germany.

References

- Baum, B. A., A. J. Heymsfield, P. Yang, and S. T. Bedka (2005a), Bulk scattering properties for the remote sensing of ice clouds: Part I. Microphysical data and models, *J. Appl. Meteorol.*, *44*(12), 1885–1895.
- Baum, B. A., P. Yang, A. J. Heymsfield, S. Platnick, M. D. King, Y. X. Hu, and S. T. Bedka (2005b), Bulk scattering properties for the remote sensing of ice clouds: Part II. Narrowband models, *J. Appl. Meteorol.*, *44*(12), 1896–1911.
- Baumgardner, D., J. E. Dye, B. W. Gandrud, and R. G. Knollenberg (1992), Interpretation of measurements made by the forward scattering spectrometer probe (FSSP-300) during the airborne arctic stratospheric expedition, *J. Geophys. Res.*, *97*(D8), 8035–8046.
- Bierwirth, E., et al. (2009), Spectral surface albedo over Morocco and its impact on the radiative forcing of Saharan dust, *Tellus Ser. A*, *61*, 252–269.
- Cess, R., S. Nemesure, E. Dutton, J. DeLuisi, G. Potter, and J.-J. Morcrette (1993), The impact of clouds on the shortwave radiation budget of the surface-atmosphere system: Interfacing measurements and models, *J. Clim.*, *6*, 308–316.
- Chang, F. L., and Z. Q. Li (2003), Retrieving vertical profiles of water-cloud droplet effective radius: Algorithm modification and preliminary application, *J. Geophys. Res.*, *108*(D24), 4763, doi:10.1029/2003JD003906.
- Chen, T., W. Rossow, and Y. Zhang (2000), Radiative effects of cloud-type variations, *J. Clim.*, *13*, 264–286.
- Chepfer, H., P. Minnis, D. Young, L. Nguyen, and R. F. Arduini (2002), Estimation of cirrus cloud effective ice crystal shapes using visible reflectances from dual-satellite measurements, *J. Geophys. Res.*, *107*(D23), 4730, doi:10.1029/2000JD000240.
- Comstock, J. M., et al. (2007), An intercomparison of microphysical retrieval algorithms for upper-tropospheric ice clouds, *Bull. Am. Meteorol. Soc.*, *88*(2), 191–204.
- Ehrlich, A., E. Bierwirth, M. Wendisch, J.-F. Gayet, G. Mioche, A. Lampert, and J. Heintzenberg (2008), Cloud phase identification of Arctic boundary-layer clouds from airborne spectral reflection measurements: Test of three approaches, *Atmos. Chem. Phys.*, *8*, 7493–7505.
- Formenti, P., and M. Wendisch (2008), Combining upcoming satellite missions and aircraft activities, *Bull. Am. Meteorol. Soc.*, *89*, 385–388.
- Francis, P., P. Hignett, and A. Macke (1998), The retrieval of cirrus cloud properties from aircraft multi-spectral reflectance measurements during EUCREX '93, *Q. J. R. Meteorol. Soc.*, *124*, 1273–1291.
- Garrett, T. J., H. Gerber, D. G. Baumgardner, C. H. Twohy, and E. M. Weinstock (2003), Small, highly reflective ice crystals in low-latitude cirrus, *Geophys. Res. Lett.*, *30*(21), 2132, doi:10.1029/2003GL018153.
- Gayet, J. F., J. Ovarlez, V. Shcherbakov, J. Strom, U. Schumann, A. Minikin, F. Aurioi, A. Petzold, and M. Monier (2004), Cirrus cloud microphysical and optical properties at southern and northern midlatitudes during the INCA experiment, *J. Geophys. Res.*, *109*, D20206, doi:10.1029/2004JD004803.
- Key, J. R., P. Yang, B. A. Baum, and S. L. Nasiri (2002), Parameterization of shortwave ice cloud optical properties for various particle habits, *J. Geophys. Res.*, *107*(D13), 4181, doi:10.1029/2001JD000742.
- King, M. D., S. Platnick, P. Yang, G. T. Arnold, M. A. Gray, J. C. Riedi, S. A. Ackerman, and K. N. Liou (2004), Remote sensing of liquid water and ice cloud optical thickness and effective radius in the Arctic: Application of airborne multispectral MAS data, *J. Atmos. Oceanic Technol.*, *21*(6), 857–875.
- Kinne, S., and K. N. Liou (1989), The effects of the nonsphericity and size distribution of ice crystals on the radiative properties of cirrus clouds, *Atmos. Res.*, *24*, 184–273.
- Klett, J. D. (1981), Stable analytical inversion solution for processing lidar returns, *Appl. Opt.*, *20*(2), 211–220.
- Knap, W., M. Hess, P. Stammes, R. Koelemeijer, and P. Watts (1999), Cirrus optical thickness and crystal size retrieval from ATSR-2 data using

- phase functions of imperfect hexagonal ice crystals, *J. Geophys. Res.*, *104*(D24), 31,721–31,730.
- Korolev, A. V., G. A. Isaac, and J. Hallett (1999), Ice particle habits in Arctic clouds, *Geophys. Res. Lett.*, *26*(9), 1299–1302.
- Labonnote, L. C., G. Brogniez, M. Doutriaux-Boucher, J. C. Buriez, J.-F. Gayet, and H. Chepfer (2000), Modeling of light scattering in cirrus clouds with inhomogeneous hexagonal monocrystals. Comparison with in-situ and ADEOS-POLDER measurements, *Geophys. Res. Lett.*, *27*(1), 113–116.
- Lawson, R. P., B. A. Baker, C. G. Schmitt, and T. L. Jensen (2001), An overview of microphysical properties of Arctic clouds observed in May and July 1998 during FIRE ACE, *J. Geophys. Res.*, *106*(D14), 14,989–15,014.
- Lawson, R. P., B. Baker, B. Pilson, and Q. X. Mo (2006), In situ observations of the microphysical properties of wave, cirrus, and anvil clouds: Part II. Cirrus clouds, *J. Atmos. Sci.*, *63*(12), 3186–3203.
- Liou, K.-N. (1986), Influence of cirrus clouds on weather and climate processes: A global perspective, *Mon. Weather Rev.*, *114*, 1167–1199.
- Lynch, D., K. Sassen, D. Starr, and G. Stephens (2002), *Cirrus*, Oxford Univ. Press, New York.
- Macke, A. (1993), Scattering of light by polyhedral ice crystals, *Appl. Opt.*, *32*(15), 2780–2788.
- Macke, A., and P. N. Francis (1998), The role of ice particle shapes and size distributions in the single scattering properties of cirrus clouds, *J. Atmos. Sci.*, *55*(17), 2874–2883.
- Mayer, B., and A. Kylling (2005), Technical note: The libRadtran software package for radiative transfer calculations—Description and examples of use, *Atmos. Chem. Phys.*, *5*, 1855–1877.
- McFarlane, S. A., and R. T. Marchand (2008), Analysis of ice crystal habits derived from MISR and MODIS observations over the ARM southern great plains site, *J. Geophys. Res.*, *113*, D07209, doi:10.1029/2007JD009191.
- McFarlane, S. A., R. T. Marchand, and T. P. Ackerman (2005), Retrieval of cloud phase and crystal habit from Multiangle Imaging Spectroradiometer (MISR) and Moderate Resolution Imaging Spectroradiometer (MODIS) data, *J. Geophys. Res.*, *110*, D14201, doi:10.1029/2004JD004831.
- McFarquhar, G., P. Yang, A. Macke, and A. Baran (2002), A new parameterization of single scattering solar radiative properties for tropical anvils using observed ice crystal size and shape distributions, *J. Atmos. Sci.*, *59*, 2458–2478.
- Nakajima, T., and M. King (1990), Determination of the optical thickness and effective particle radius of clouds from reflected solar radiation measurements: Part I. Theory, *J. Atmos. Sci.*, *47*, 1878–1893.
- Nasiri, S. L., B. A. Baum, A. J. Heymsfield, P. Yang, M. R. Poellot, D. P. Kratz, and Y. X. Hu (2002), The development of midlatitude cirrus models for modis using fire-i, fire-ii, and arm in situ data, *J. Appl. Meteorol.*, *41*(3), 197–217.
- Ou, S., K. Liou, W. Gooch, and Y. Takano (1993), Remote sensing of cirrus cloud parameters using advanced very-high-resolution radiometer 3.7- and 10.9- μm channels, *Appl. Opt.*, *32*, 2171–2180.
- Platnick, S. (2000), Vertical photon transport in cloud remote sensing problems, *J. Geophys. Res.*, *105*(D18), 22,919–22,935.
- Platnick, S., M. King, S. Ackerman, W. Menzel, B. Baum, J. Riedi, and R. Frey (2003), The MODIS cloud products: Algorithms and examples from TERRA, *IEEE Trans. Geosci. Remote Sens.*, *41*, 459–473.
- Ricchiazzi, P., S. Yang, C. Gautier, and D. Sowle (1998), SBDART: A research and teaching software tool for plane-parallel radiative transfer in the Earth's atmosphere, *Bull. Am. Meteorol. Soc.*, *79*, 2101–2114.
- Rolland, P., K. Liou, M. King, S. Tsay, and G. McFarquhar (2000), Remote sensing of optical and microphysical properties of cirrus clouds using Moderate-Resolution Imaging Spectroradiometer channels: Methodology and sensitivity to physical assumptions, *J. Geophys. Res.*, *105*(D9), 11,721–11,738.
- Schaaf, C. B., et al. (2002), First operational BRDF, albedo nadir reflectance products from MODIS, *Remote Sens. Environ.*, *83*(1–2), 135–148.
- Schmitt, C. G., and A. J. Heymsfield (2007), On the occurrence of hollow bullet rosette- and column-shaped ice crystals in midlatitude cirrus, *J. Atmos. Sci.*, *64*(12), 4514–4519.
- Stamnes, K., S. Tsay, W. Wiscombe, and K. Jayaweera (1988), A numerically stable algorithm for discrete-ordinate-method radiative transfer in multiple scattering and emitting layered media, *Appl. Opt.*, *27*(12), 2502–2509.
- Stephens, G., S.-C. Tsay, P. Stackhouse Jr., and P. Flatau (1990), The relevance of the microphysical and radiative properties of cirrus clouds to climate and climatic feedback, *J. Atmos. Sci.*, *47*, 1742–1753.
- Stephens, G., et al. (2002), The CloudSat mission and the A-train, *Bull. Am. Meteorol. Soc.*, *83*, 1771–1790.
- Takano, Y., and K.-N. Liou (1989), Solar radiative transfer in cirrus clouds: Part I. Single-scattering and optical properties of hexagonal ice crystals, *J. Atmos. Sci.*, *46*, 1–19.
- Twomey, S., and K. J. Seton (1980), Inferences of gross microphysical properties of clouds from spectral reflectance measurements, *J. Atmos. Sci.*, *37*, 1065–1069.
- Wendisch, M., D. Müller, D. Schell, and J. Heintzenberg (2001), An airborne spectral albedometer with active horizontal stabilization, *J. Atmos. Oceanic Technol.*, *18*(11), 1856–1866.
- Wendisch, M., P. Pilewskie, E. Jäkel, S. Schmidt, J. Pommier, S. Howard, H. H. Jonsson, H. Guan, M. Schroder, and B. Mayer (2004), Airborne measurements of areal spectral surface albedo over different sea and land surfaces, *J. Geophys. Res.*, *109*, D08203, doi:10.1029/2003JD004392.
- Wendisch, M., P. Pilewskie, J. Pommier, S. Howard, P. Yang, A. J. Heymsfield, C. G. Schmitt, D. Baumgardner, and B. Mayer (2005), Impact of cirrus crystal shape on solar spectral irradiance: A case study for subtropical cirrus, *J. Geophys. Res.*, *110*, D03202, doi:10.1029/2004JD005294.
- Wirth, M., A. Fix, P. Mahnke, H. Schwarzer, F. Schrandt, and G. Ehart (2009), The airborne multi-wavelength water vapor differential absorption lidar WALES: System design and performance, *Appl. Phys. B*, *96*, 201–213.
- Wyser, K. (1999), Ice crystal habits and solar radiation, *Tellus Ser. A*, *51*(5), 937–950.
- Yang, P., K. N. Liou, K. Wyser, and D. Mitchell (2000), Parameterization of the scattering and absorption properties of individual ice crystals, *J. Geophys. Res.*, *105*(D4), 4699–4718.
- Yang, P., G. Hong, G. W. Kattawar, P. Minnis, and Y. Hu (2008), Uncertainties associated with the surface texture of ice particles in satellite-based retrieval of cirrus clouds: Part II. Effect of particle surface roughness on retrieved cloud optical thickness and effective particle size, *IEEE Trans. Geosci. Remote Sens.*, *46*, 1948–1957.
- Zhang, Y., A. Macke, and F. Albers (1999), Effect of crystal size spectrum and crystal shape on stratiform cirrus radiative forcing, *Atmos. Res.*, *52*(1–2), 59–75.

A. Ehrlich and M. Wendisch, Institut für Meteorologie, Universität Leipzig, Stephanstr. 3, D-04103 Leipzig, Germany. (a.ehrlich@uni-leipzig.de; m.wendisch@uni-leipzig.de)

H. Eichler, Institut für Physik der Atmosphäre, Johannes Gutenberg-Universität Mainz, Becherweg 21, D-55099 Mainz, Germany. (eichlerh@uni-mainz.de)

C. Emde, A. Minikin, and M. Wirth, Institut für Physik der Atmosphäre, Deutsches Zentrum für Luft- und Raumfahrt Oberpfaffenhofen, München Str. 20, 82234 Wessling, Germany. (claudia.emde@dlr.de; andreas.minikin@dlr.de; martin.wirth@dlr.de)

J.-F. Gayet and G. Mioche, Laboratoire de Météorologie Physique, Université Blaise Pascal, Avenue des Landais, F-63177 Aubière, France. (j.f.gayet@opgc.univ-bpclermont.fr; g.mioche@opgc.univ-bpclermont.fr)